The significance of the evanescent spectrum in structure-waveguide interaction problems

Apostolos Tsouvalas,[a] Karel N. van Dalen, and Andrei V. Metrikine
Faculty of Civil Engineering and Geosciences, Delft University of Technology, Stevinweg 1, 2628 CN, Delft, The Netherlands

(Received 20 January 2015; accepted 15 September 2015; published online 30 October 2015)

Modal decomposition is often applied in elastodynamics and acoustics for the solution of problems related to propagation of mechanical disturbances in waveguides. One of the key elements of this method is the solution of an eigenvalue problem for obtaining the roots of the dispersion equation, which signify the wavenumbers of the waves that may exist in the system. For non-dissipative media, the wavenumber spectrum consists of a finite number of real roots supplemented by infinitely many imaginary and complex ones. The former refer to the propagating modes in the medium, whereas the latter constitute the so-called evanescent spectrum. This study investigates the significance of the evanescent spectrum in structure-waveguide interaction problems. Two cases are analysed, namely, a beam in contact with a fluid layer and a cylindrical shell interacting with an acousto-elastic waveguide. The first case allows the introduction of a modal decomposition method and the establishment of appropriate criteria for the truncation of the modal expansions in a simple mathematical framework. The second case describes structure-borne wave radiation in an offshore environment during the installation of a pile with an impact hammer—a problem that has raised serious concerns in recent years due to the associated underwater noise pollution.
© *2015 Acoustical Society of America*. [http://dx.doi.org/10.1121/1.4932016]

[AJH] Pages: 2574–2588

I. INTRODUCTION

Modal decomposition is often used for the solution of problems related to wave propagation in acoustic, elastic, or acousto-elastic waveguides. The continuous interest in these problems is created by numerous applications of practical interest in the field of non-destructive material characterisation,[1,2] structural acoustics,[3,4] geophysics,[5,6] and seismology.[7] The solution to the system of equations describing propagation of mechanical disturbances in waveguides requires the simultaneous satisfaction of a system of equations of motion together with a number of boundary and interface conditions. It is well-known that a non-trivial solution exists for discrete values of the wavenumber k, which being a function of the excitation frequency ω, describes the propagation or decay parallel to the boundaries of the waveguide. These values of k can be found by solving a classical eigenvalue problem.

Whereas the solution of such eigenvalue problems is rather straightforward for acoustic waveguides,[8] this is not the case for elastic or porous layered media. The main difficulty in the latter cases arises from the fact that complex eigenvalues do exist even for the undamped media.[9] When wave propagation in layered media is considered, there is first the challenge that infinitely many roots exist and, second, that these roots are closely spaced in the complex plane. To date, the focus is almost solely placed on the real-valued roots which correspond to propagating modes in the waveguide. Consequently, investigations into the significance of the evanescent spectrum for structure-waveguide interaction problems are scarce. This study aims to fill this gap.

In the literature, numerous publications exist in which the propagation of mechanical disturbances in waveguides is treated in detail, but only a few of them investigate the complete wave spectrum. Achenbach[9] has investigated the complete wave spectrum of an elastic layer with stress-free surfaces, pointing out the existence of complex-valued roots even for the undamped medium. Karp and Durban[10] examined the complete wave field of a pre-stretched hyperelastic plate focusing on the numerical findings for the complex wavenumbers associated with evanescent waves. In the field of non-destructive material characterisation, the modal decomposition is often favoured. Shkerdin and Glorieux[1,2] have investigated Lamb mode propagation through a composite plate consisting of two parallel layers of different materials with a finite length delamination. The method to calculate the transmitted and reflected fields was based on a modal expansion of each field in terms of propagating and evanescent modes. The adopted solution method allowed for an error estimation based on the number of evanescent modes considered in the modal expansions. In a more recent paper, Shkerdin and Glorieux[11] treated the interaction of Lamb modes in a steel plate with a thin inclusion and reported the importance of the evanescent spectrum. Nennig *et al.*[12] applied a mode matching method for predicting the transmission loss of a cylindrically shaped dissipative silencer partially filled with a poroelastic foam. The method of solution was very similar to that of Shkerdin and Glorieux,[1] but the integral formulation was obtained by using arbitrarily chosen weighting functions rather than the orthogonality relation of the modal expansions. Modal methods have also been extensively used in the field of geophysics and seismology. In one of the few publications in which the complete

[a]Electronic mail: a.tsouvalas@tudelft.nl

Redistribution subject to ASA license or copyright; see http://acousticalsociety.org/content/terms. Download to IP: 131.180.130.187 On: Mon, 30 Nov 2015 07:29:08

wave spectrum is considered, Stange and Friederich[5,6] investigated wave propagation in waveguides with sharp lateral heterogeneities using a modal decomposition approach. Their work highlighted the importance of the evanescent modes for the satisfaction of the displacement and stress continuity at the various interfaces.

The examples discussed above consider wave propagation in waveguides with several internal discontinuities. To this end, the source of the radiated wave field is usually simple and *a priori* defined. On the contrary, the present study focuses on a modal decomposition method applied in structure-waveguide interaction problems in which a structure that is in full contact with the waveguide is subjected to a dynamic excitation. In such systems, the dynamic behaviour of the structure and the accuracy of the solution to the coupled problem define the actual source mechanism that is responsible for the radiated field into the waveguide. In this context, the contribution of the evanescent field seems to be more pronounced. Two systems are investigated: (i) a beam in contact with a fluid layer and (ii) a cylindrical shell embedded in a layered acousto-elastic waveguide. The modal decomposition method is applied for each subsystem, i.e., the structural domain and the waveguide. The modal coefficients are then determined by an appropriate combination of the kinematic conditions at the interface of the two domains and the use of the orthogonality relations of each set of eigenmodes. Thus, the solution to the problem is semi-analytical and the only approximation employed is on the truncation of the modal expansions to reduce the infinite set of linear algebraic equations. This study focuses on the choice of a proper truncation scheme that is based on the contribution of the evanescent spectrum on the resulting displacements and stresses in the structure and in the waveguide.

The paper is structured as follows. Section II introduces the theoretical background of the method by examining the vibrations of a beam in contact with a fluid layer. The significance of the evanescent spectrum is emphasised together with the establishment of appropriate truncation criteria of the modal expansions. In Sec. III, the case of a cylindrical shell in contact with an acousto-elastic medium is analysed. Finally, Sec. IV focuses on the practical case of a steel pile being driven into the soil offshore. This particular example is chosen here because it recently received the attention of the acoustic specialists throughout the world.[13–16] Sound radiation generated during the installation of piles emits strong impulsive sounds into the seawater column, which can be harmful for the marine ecosystem. With today's increasing concern regarding the environmental impact of such operations, it is of high importance to provide engineering tools for reliable predictions of the underwater noise levels.

II. THEORETICAL BACKGROUND

The theoretical background is introduced with the help of a one-dimensional continuum coupled to an acoustic layer. The chosen example is shown in Fig. 1 and consists of an elastically supported beam in contact with a fluid layer. The beam is of finite length, i.e., $0 \le x \le L$, and the fluid occupies the region $y \ge 0$ and $0 \le x \le L$. EI, ρ_b, and k_d define the bending stiffness, the mass per unit of length of the beam, and the spring constant, respectively. In the fluid region, ρ_f and c_f define the density and wave speed, respectively. At $x = 0, L$, the displacement of the beam along the y– direction is restrained and the rotation is free. Finally, the fluid layer is bounded by a pressure release surface at $x = 0$ and by a rigid bottom at $x = L$. Other boundary conditions can also be treated within the framework of the present method, but the simplest possible choice is adopted here for the purpose of this study.

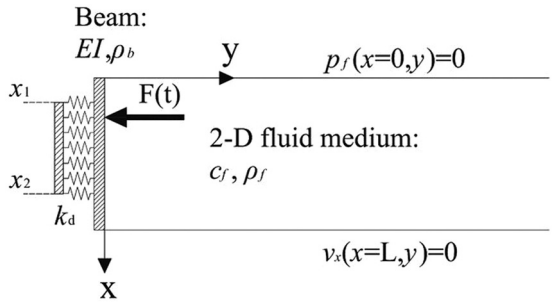

FIG. 1. Geometry of an elastically supported beam in contact with an acoustic fluid. The beam is subjected to a point force at $x = x_0$. The beam vibrations excite acoustic waves in the fluid region.

A. Governing equations and analytical solution

The governing equations describing the linear vibrations of the coupled beam-fluid system in the frequency domain are

$$EI\frac{d^4\tilde{w}(x)}{dx^4} - \omega^2\rho_b\,\tilde{w}(x) + \big(H(x-x_1) - H(x-x_2)\big)\,k_d\,\tilde{w}(x) = -\tilde{F}(\omega)\,\delta(x-x_0) - \tilde{p}_f(x, y=0), \tag{1}$$

$$\nabla^2\tilde{\chi}(x,y) + \kappa_f^2\,\tilde{\chi}(x,y) = 0, \tag{2}$$

$$\tilde{w}(x=0) = \tilde{w}(x=L) = 0, \tag{3}$$

$$\left\{\frac{d^2\tilde{w}(x)}{dx^2}\right\}_{x=0} = \left\{\frac{d^2\tilde{w}(x)}{dx^2}\right\}_{x=L} = 0, \tag{4}$$

$$\tilde{p}_f(x=0,y) = 0 \rightarrow -\mathrm{i}\omega\rho_f\,\tilde{\chi}(x=0,y) = 0, \tag{5}$$

$$\tilde{v}_x(x=L,y) = 0 \rightarrow \left\{\frac{\partial\tilde{\chi}(x,y)}{\partial x}\right\}_{x=L} = 0, \tag{6}$$

$$\tilde{v}_y(x,y=0) = \mathrm{i}\omega\tilde{w}(x) \rightarrow \left\{\frac{\partial\tilde{\chi}(x,y)}{\partial y}\right\}_{y=0} = \mathrm{i}\omega\tilde{w}(x). \tag{7}$$

In the equations above, $\tilde{w}(x)$ is the displacement of the beam, $\tilde{p}_f(x,y)$ denotes the pressure of the fluid, $\tilde{\chi}(x,y)$ is a velocity potential and $\tilde{v}_x(x,y)$, $\tilde{v}_y(x,y)$ are the particle velocities of the fluid in the vertical and horizontal directions, respectively. In addition, $\tilde{F}(\omega)$ denotes the Fourier transform of the force $F(t)$ applied at $x = x_0$, $\kappa_f^2 = \omega^2/c_f^2$, and $\nabla^2 = \partial^2/\partial x^2 + \partial^2/\partial y^2$. The frequency domain is related to

Redistribution subject to ASA license or copyright; see http://acousticalsociety.org/content/terms. Download to IP: 131.180.130.187 On: Mon, 30 Nov 2015 07:29:08

the time domain through the integral Fourier transform $\tilde{g}(\omega) = \int_{-\infty}^{+\infty} g(t)\, \exp(-\mathrm{i}\omega t)\, d\omega$, in which $g(t)$ and $\tilde{g}(\omega)$ denote the quantity of interest in the time and in the frequency domain, respectively.

First, the response of the beam and the fluid are expressed in terms of modes,[17] which satisfy the boundary conditions at $x=0$ and $x=L$, as well as the condition of finite response at infinite distance from the source (i.e., $y \to +\infty$ for the fluid layer)

$$\tilde{w}(x) = \sum_{n=1}^{\infty} A_n \sin\left(\frac{n\pi x}{L}\right), \tag{8}$$

$$\tilde{\chi}(x,y) = \sum_{m=0}^{\infty} C_m \sin(k_{x,m}x)\, \exp(-\mathrm{i}\, k_{y,m}\, y), \tag{9}$$

in which A_n and C_m are unknown modal coefficients of the beam and the fluid, respectively, to be determined by the solution of the forced equation. Similarly, $k_{x,m} = (2m+1)\pi/2L$ and $k_{y,m} = \sqrt{\kappa_f^2 - k_{x,m}^2}$ are the vertical and horizontal wavenumbers in the fluid domain, respectively. For the wavenumbers in the horizontal direction, we require that $\mathrm{Re}(k_{y,m}) \geq 0$ or $\mathrm{Im}(k_{y,m}) \leq 0$, depending on $k_{y,m}$ being real or imaginary. Obviously, the modal sets for the fluid and the beam are different.

Second, by using Eq. (7), expanding both the fluid and beam displacements in terms of Eqs. (8) and (9), multiplying by another fluid mode, i.e., $\sin(k_{x,k}x)$, and applying the orthogonality of the fluid modes, the coefficients A_n and C_m can be interrelated. Thus, the fluid pressure exerted on the beam can be expressed in terms of the modal coefficients of the beam as

$$\tilde{p}_f(x, y=0) = \mathrm{i}\omega^2 \rho_f \sum_{n=1}^{\infty} A_n \sum_{m=0}^{\infty} \frac{R_{nm}}{k_{y,m}} \sin(k_{x,m}x), \tag{10}$$

in which

$$R_{nm} = \int_0^L \sin\left(\frac{n\pi\bar{x}}{L}\right) \sin(k_{x,m}\bar{x})\, d\bar{x}. \tag{11}$$

Note that the fluid modes are normalized so that $\int_0^L \sin^2(k_{x,m}x)\, dx = 1$. Substituting Eq. (10) into Eq. (1), multiplying both sides by another beam mode, i.e., $\sin(l\pi x/L)$, and applying the orthogonality of beam modes, yields an infinite set of coupled algebraic equations

$$\sum_{n=1}^{\infty} (\rho_b(\omega_n^2 - \omega^2)\delta_{nl} + K_{nl} - Z_{nl})\, A_n = F_l, \tag{12}$$

in which

$$K_{nl} = k_d \int_{x_1}^{x_2} \sin\left(\frac{n\pi x}{L}\right) \sin\left(\frac{l\pi x}{L}\right) dx, \tag{13}$$

$$Z_{nl} = \sum_{m=0}^{\infty} \frac{\mathrm{i}\omega^2 \rho_f R_{lm}}{k_{y,m}} \int_0^L \sin\left(\frac{n\pi x}{L}\right) \sin(k_{x,m}x)\, dx, \tag{14}$$

$$F_l = -\tilde{F}(\omega) \sin\left(\frac{l\pi x_0}{L}\right). \tag{15}$$

In Eq. (12), δ_{nl} is the Kronecker delta, Z_{nl} denotes the impedance of the fluid, and ω_n is the eigenfrequency of the beam for mode n. Note also that a visco-elastic support (with c_d being the viscous coefficient) can be treated in a similar way with merely a substitution of k_d in Eq. (13) by $k_d + \mathrm{i}\omega c_d$. Equation (12) can be solved for obtaining the unknown modal coefficients A_n. In order to solve the infinite system of linear equations, the modal expansions of both subsystems (beam and fluid) need to be truncated. Whereas for the beam modes an estimation of the upper limit of the modal expansion can be based on the maximum frequency of the load, for the fluid modes the choice is not that obvious. The choice of a proper truncation scheme for the fluid modes is the subject of discussion in Sec. II B.

B. Truncation of the modal expansions

A numerical example is analysed in this section. The force is applied at $x_0 = L/3$ with an amplitude of $|\tilde{F}(\omega)| = 10^6$ N s. The geometrical and material properties of the systems are defined in accordance with Fig. 1: $L = 10\,\mathrm{m}$, $x_1 = 0.2L$, $x_2 = 0.9L$, $EI = 7.2 \times 10^6\,\mathrm{N\,m^{-2}}$, $\rho_b = 300\,\mathrm{kg\,m^{-1}}$, $k_d = 10^5\,\mathrm{N\,m^{-2}}$, $\rho_f = 1000\,\mathrm{kg\,m^{-3}}$, and $c_f = 1500\,\mathrm{m\,s^{-1}}$. In the results presented hereafter, the number of beam modes considered in the modal expansion is 100, which is regarded to be sufficient for the considered range of frequencies $0 \leq f \leq 500$ Hz. The roots of the dispersion equation of the fluid layer are given by $k_{y,m} = \sqrt{\kappa_f^2 - ((2m+1)\pi/2L)^2}$, with $m = 0, 1, \ldots, \infty$. Consequently, the eigenvalues can be either real (propagating modes) or imaginary (evanescent modes).

In order to illustrate the significance of the evanescent modes in the solution of the coupled problem, the satisfaction of the kinematic condition at the beam-fluid interface, i.e., Eq. (7), is first examined. In Figs. 2(a)–2(c), the modulus of the displacement amplitude of the beam $|\tilde{w}| = \sqrt{(\mathrm{Re}\{\tilde{w}\})^2 + (\mathrm{Im}\{\tilde{w}\})^2}$ and the fluid $|\tilde{u}_y| = \sqrt{(\mathrm{Re}\{\tilde{u}_y\})^2 + (\mathrm{Im}\{\tilde{u}_y\})^2}$ with $\tilde{u}_y = \tilde{v}_y/(\mathrm{i}\omega)$, are plotted together with the mismatch of the two at the interface $y=0$ at $f = 0.5$ kHz for a varying number of evanescent modes included in the modal summation. At this frequency, seven propagating modes exist in the fluid layer. As can be seen, the inclusion of a small number of evanescent modes suffices for a substantial improvement of the fit at the interface. In addition, the convergence of the interface condition improves monotonically as the number of evanescent modes increases. The mismatch of the displacements when only the propagating modes are considered in the modal summation is large.

Based on these results, a convergence criterion is adopted for the displacement mismatch error $\delta(x)$ along the length of the beam, i.e., at $y=0$,

$$\delta(x) = \left| \frac{\tilde{w}(x) - \tilde{u}_y(x, y=0)}{\tilde{w}(x)} \right|. \tag{16}$$

Redistribution subject to ASA license or copyright; see http://acousticalsociety.org/content/terms. Download to IP: 131.180.130.187 On: Mon, 30 Nov 2015 07:29:08

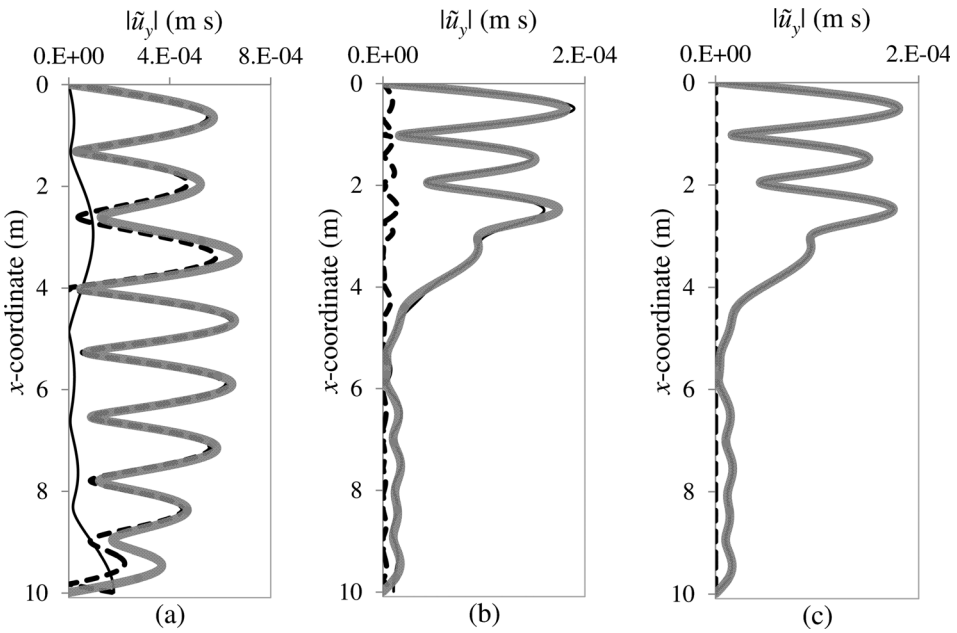

FIG. 2. Horizontal displacement mismatch at the beam-fluid interface at $f = 500$ Hz for different amounts of evanescent modes included in the solution. In (a), only the propagating modes are included. In (b) and (c), 6 and 100 evanescent modes are included, respectively. The thin line denotes the fluid displacement, the thick grey line denotes the beam displacement, and the dashed line denotes the mismatch of these two. The inclusion of a larger number of evanescent modes of the acoustic layer reduces the mismatch of the displacements at the beam-fluid interface.

The average displacement mismatch error can be obtained as $\hat{\delta}_u = \langle \delta(x) \rangle$, in which $\langle \cdot \rangle$ denotes here the average displacement mismatch along the length of the beam. In Fig. 3, $\hat{\delta}_u$ is plotted as a function of the number of evanescent modes considered in the modal expansion for frequencies up to 500 Hz. As can be seen, the average displacement error is larger than 10% when <20 evanescent modes are considered at all frequencies and drops below 1% only when more than 80 evanescent modes are included. With 100 evanescent modes, $\hat{\delta}_u < 0.5\%$ throughout the frequency range, which verifies the results shown in Fig. 2(c). In Fig. 4, the distributed bending moment $\tilde{M}(x) = -EI\,(d^2\tilde{w}(x)/dx^2)$ and the shear force $\tilde{V}(x) = d\tilde{M}/dx$ along the beam length are shown at $f = 500$ Hz for a varying number of evanescent modes considered. The convergence of the bending moment and shear force are rather well represented by the displacement mismatch error at the interface. In other words, the check of the displacement convergence at the interface suffices for an accurate prediction of the bending moment and shear force in the beam.

Apart from the displacement continuity at the beam-fluid interface, it is of interest to investigate the influence of the inclusion of a progressively larger number of evanescent modes on the calculation of the modal coefficients of propagating modes of the fluid C_m. Since the radiated acoustic power depends solely on the propagating modes (the evanescent modes *carry* no energy through a surface positioned away from the interface), any error in the estimation of the modal amplitudes of the propagating modes will be reflected in the energy radiated into the fluid region. For convenience, we introduce the error $\delta_{p,m}$ in the estimation of the coefficient of the propagating mode m as follows:

$$\delta_{p,m} = \left| \frac{C_m - C_m^a}{C_m^a} \right|, \tag{17}$$

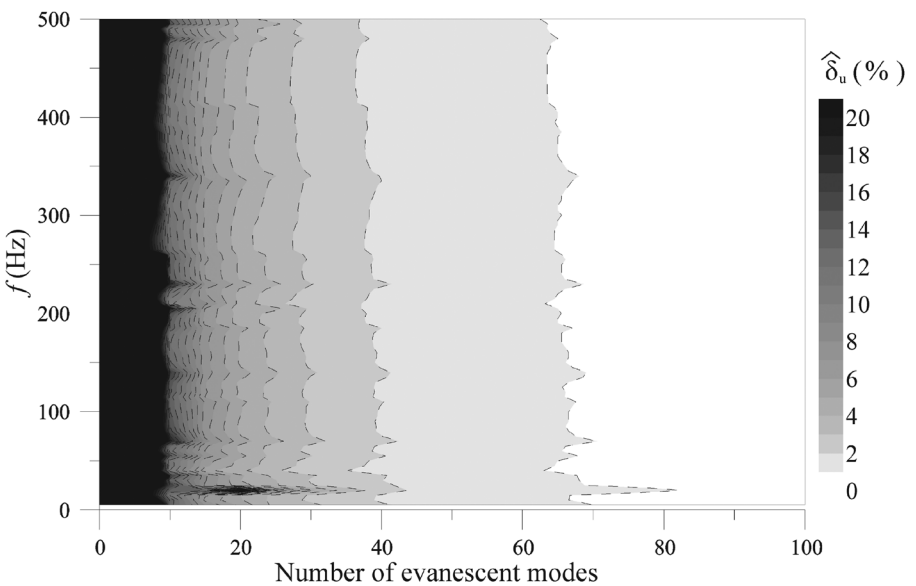

FIG. 3. Contour plot of the average displacement error $\hat{\delta}_u$ (%) at the beam-fluid interface as a function of the number of the evanescent modes (horizontal axis) and the excitation frequency (vertical axis). The inclusion of more than 80 evanescent modes limits the error below 2% at the frequency range $0 \leq f \leq 500$ Hz.

Redistribution subject to ASA license or copyright; see http://acousticalsociety.org/content/terms. Download to IP: 131.180.130.187 On: Mon, 30 Nov 2015 07:29:08

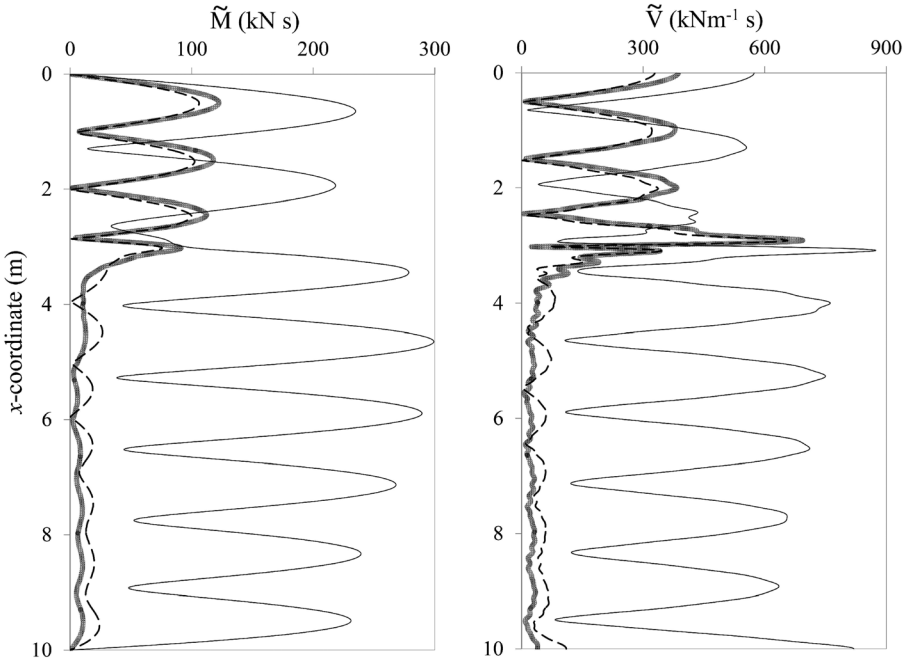

FIG. 4. Bending moment (left) and shear force (right) in the beam at $f = 0.5$ kHz. The continuous line corresponds to the case in which only propagating modes are considered. The dashed line and the thick grey line correspond to the situation in which 4 and 100 evanescent modes are included, respectively. Again, the inclusion of a large number of evanescent modes is required for the correct prediction of the forces and moments in the beam structure.

in which $\delta_{p,m}$ denotes the error in the estimation of the propagating mode coefficient C_m and C_m^a denotes the same coefficient evaluated by including 200 evanescent modes in the modal expansion. The average displacement error in the latter case equals $\hat{\delta}_u \simeq 0.05\%$ and is considered hereafter as the exact solution to the problem. In Table I, the error $\delta_{p,m}$ with $m = 1, 2, ..., 7$ (seven propagating modes) is shown for a varying number of evanescent modes at $f = 500$ Hz. As can be seen, the convergence of the coefficients of the propagating modes to within an error of $<1\%$ requires the inclusion of only ten evanescent modes.

The displacement error defined by Eq. (16) is larger than the error of the propagating modes given by Eq. (17) when the same number of evanescent modes is considered in the solution of Eq. (12). The former is associated with the satisfaction of the displacement continuity at the beam-fluid interface. On the contrary, the latter is associated with energy radiation into the fluid for which a correct estimation of the coefficients of the propagating modes alone suffices. However, when one is interested in the resulting bending moments and shear forces in the structure (as well as the near-field intensity of the acoustic field), the displacement error criterion seems to be more appropriate since it inherently provides the necessary error estimation in the calculation of the coefficients of the evanescent modes.

TABLE I. Error $\delta_{p,m}(\%)$ in the estimation of the coefficients of the propagating modes at $f = 500$ Hz. When only propagating modes of the acoustic layer are considered, the introduced error is large. With the inclusion of a small fraction of the evanescent spectrum, i.e., ten evanescent modes, the error in the estimation of the propagating-mode coefficients is limited to a value $<1\%$.

Evanescent modes	$\delta_{p,1}$	$\delta_{p,2}$	$\delta_{p,3}$	$\delta_{p,4}$	$\delta_{p,5}$	$\delta_{p,6}$	$\delta_{p,7}$
0	>100	92.62	>100	>100	>100	>100	>100
2	38.69	19.70	26.30	>100	24.28	23.96	>100
4	15.59	7.933	10.56	42.54	9.694	9.536	69.22
6	0.808	0.410	0.543	2.169	0.489	0.477	3.427
8	0.474	0.240	0.319	1.275	0.288	0.281	2.023
10	0.176	0.089	0.118	0.468	0.105	0.101	0.721
20	0.016	0.008	0.010	0.042	0.009	0.008	0.063
100	0.000	0.000	0.000	0.000	0.000	0.000	0.000

III. CYLINDRICAL SHELL COUPLED TO AN ACOUSTO-ELASTIC MEDIUM

In Sec. II, the simple case of a beam vibrating in a fluid column was investigated. The beam-fluid model allowed us to highlight the importance of the evanescent modes in the correct determination of the shear forces and bending modes in the beam, and to develop appropriate criteria for the convergence of the solution. In this section, the case of a cylindrical shell in full contact with an acousto-elastic waveguide is considered. A similar model has been developed for predictions of structure-borne wave radiation by offshore pile driving by Tsouvalas and Metrikine.[4] In the sequel, an extension of the original model for a layered system is presented and the convergence of the solution for various modal truncation schemes is examined.

A. Governing equations and modal decomposition

The total system consists of the shell and the layered acousto-elastic domain as shown in Fig. 5. The system is excited by a force applied at the top side of the shell. A linear high-order shell theory is considered for the description of the shell dynamics.[18] The shell is of finite length and occupies the domain $0 \leq z \leq L$. The constants E, v, R, ρ, and $2h$ correspond to the complex modulus of elasticity in the frequency domain, the Poisson ratio, the radius of the mid-surface of the shell, the density, and the thickness of the shell, respectively. The fluid is modeled as a three-dimensional inviscid compressible medium with a pressure release boundary at $z = z_0$ and occupies the domain $z_0 \leq z$

Redistribution subject to ASA license or copyright; see http://acousticalsociety.org/content/terms. Download to IP: 131.180.130.187 On: Mon, 30 Nov 2015 07:29:08

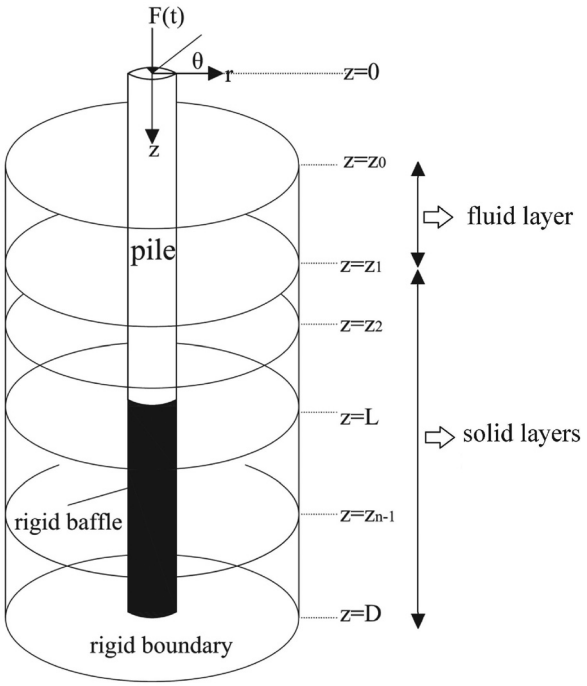

FIG. 5. Geometry of a cylindrical shell structure coupled to a layered acousto-elastic medium. The fluid layer occupies the region $z_0 < z < z_1$ and $r > R$, whereas the solid layers are horizontally stratified in the region $z_1 < z < D$ and $r > R$. This model can be used for the prediction of the structure-borne wave radiation during the installation of a pile by an impact hammer or a vibratory device.

$\leq z_1$ and $r > R$. The layered solid domain is described as a three-dimensional elastic continuum in $z_1 < z < D$ and $r > R$. The interface at $z = D$ is substituted by a rigid boundary. All layers are horizontally stratified and are distinguished by the index $j = 1, 2, ..., n$. The constants λ_j and G_j define the *Lamé* coefficients for each solid layer and ρ_j is the soil density. The various solid layers are in full contact with each other at the horizontal interfaces. At the interface with the fluid only the vertical stress equilibrium and the vertical displacement continuity are imposed (the shear stresses at the surface of the upper solid layer are set equal to zero). The shell structure is extended by a *rigid baffle* in the region $L < z < D$ to comply with the homogeneity of the domain along the z– coordinate at $r > R$.

The following set of partial differential equations govern the linear dynamics of the coupled system in the frequency domain for the cylindrically symmetric case:

$$\mathbf{L}\tilde{\mathbf{u}}_p + \mathbf{I}_m\tilde{\mathbf{u}}_p = -(H(z-z_1) - H(z-L))\tilde{\mathbf{t}}_s + (H(z-z_0) - H(z-z_1))\tilde{\mathbf{p}}_f + \tilde{\mathbf{f}}, \quad (18)$$

$$G_j\nabla^2\tilde{\mathbf{u}}_s^j + (\lambda_j + G_j)\nabla\nabla\cdot\tilde{\mathbf{u}}_s^j + \omega^2\rho_j\tilde{\mathbf{u}}_s^j = 0, \quad (19)$$

$$\nabla^2\tilde{\phi}_f(r,z,\omega) + \frac{\omega^2}{c_f^2}\tilde{\phi}_f(r,z,\omega) = 0. \quad (20)$$

In the equations above, $\tilde{\mathbf{u}}_p = [\tilde{u}_{p,z}(z,\omega)\,\tilde{u}_{p,r}(r,\omega)]^T$ is the displacement vector of the mid-surface of the shell, $\mathbf{u}_s^j(r,z,\omega) = [u_{s,z}^j(r,z,\omega),\, u_{s,r}^j(r,z,\omega)]^T$ is the displacement vector of each solid layer, and $\tilde{\phi}_f(r,z,\omega)$ is a velocity potential introduced for the description of the fluid layer. The subscripts s and f correspond to the solid and the fluid, respectively. The operators $\mathbf{L}$ and $\mathbf{I}_m$ are the stiffness and modified inertia matrices of the shell, respectively.[4] The term $\tilde{\mathbf{p}}_f$ represents the fluid pressure exerted at the outer surface of the shell at $z_0 \leq z \leq z_1$. The functions $H(z - z_i)$ are the Heaviside step functions which are used here to account for the fact that the soil and the fluid are in contact with different segments of the shell. The vector $\tilde{\mathbf{f}} = [\tilde{f}_{rz}(z,\omega)\,\tilde{f}_{rr}(z,\omega)]^T$ represents the externally applied force on the surface of the shell. The term $\tilde{\mathbf{t}}_s$ represents the boundary stress vector that takes into account the reaction of the soil surrounding the shell at $z_1 < z < L$, i.e.,

$$\tilde{\mathbf{t}}_s^j = \lambda_j\nabla\cdot\tilde{\mathbf{u}}_s^j\mathbf{I} + G_j(\nabla\tilde{\mathbf{u}}_s^j + (\nabla\tilde{\mathbf{u}}_s^j)^T), \quad (21)$$

in which j is used here to distinguish between the layers and $\mathbf{I}$ is the identity matrix. The Helmholtz decomposition is applied, i.e., $\tilde{\mathbf{u}}_s^j = \nabla\tilde{\phi}^j + \nabla\times\tilde{\boldsymbol{\psi}}^j$, in which two potentials $\tilde{\phi}^j(r,z,\omega)$ and $\tilde{\boldsymbol{\psi}}^j = [0,\, \tilde{\psi}^j(r,z,\omega),\, 0]^{\mathrm{T}}$ suffice for determining the wave field in each solid layer

$$\nabla^2\tilde{\phi}^j(r,z,\omega) + k_{L,j}^2\tilde{\phi}^j(r,z,\omega) = 0, \quad (22)$$

$$\nabla^2\tilde{\psi}^j(r,z,\omega) - \frac{\tilde{\psi}(r,z,\omega)}{r^2} + k_{T,j}^2\tilde{\psi}^j(r,z,\omega) = 0, \quad (23)$$

with $k_{L,j}^2 = \omega^2/c_{L,j}^2$ and $k_{T,j}^2 = \omega^2/c_{T,j}^2$, in which $c_{L,j}$ and $c_{T,j}$ denote the speeds of the compressional and shear waves in layer j, respectively. In addition, a set of boundary conditions at $z = 0$, $z = D$ and a set of interface conditions between the adjacent layers should be satisfied, together with the interface conditions at the shell surface

$$\tilde{p}_f(r,z_0,\omega) = 0, \quad r \geq R, \quad (24)$$

$$\tilde{\sigma}_{s,zz}^1(r,z_1,\omega) + \tilde{p}_f(r,z_1,\omega) = 0, \quad r \geq R, \quad (25)$$

$$\tilde{\sigma}_{s,zr}^1(r,z_1,\omega) = 0, \quad r \geq R, \quad (26)$$

$$\tilde{u}_{s,z}^1(r,z_1,\omega) - \tilde{v}_{f,z}(r,z_1,\omega)/(\mathrm{i}\omega) = 0, \quad r \geq R, \quad (27)$$

$$\sigma_{s,zi}^{j+1}(r,z_j,\omega) - \sigma_{s,zi}^j(r,z_j,\omega) = 0, \quad 2 \leq j \leq n-1, \quad i = z,r, \quad (28)$$

$$\tilde{u}_{s,i}^{j+1}(r,z_j,\omega) - \tilde{u}_{s,i}^j(r,z_j,\omega) = 0, \quad 2 \leq j \leq n-1, \quad i = z,r, \quad (29)$$

$$\tilde{u}_{s,r}^n(r,D,\omega) = \tilde{u}_{s,z}^n(r,D,\omega) = 0, \quad (30)$$

$$\tilde{u}_{p,r}(z,\omega) - \tilde{v}_{f,r}(R,z,\omega)/(\mathrm{i}\omega) = 0, \quad z_0 < z < z_1, \quad (31)$$

$$\tilde{u}_{p,i}(z,\omega) - \tilde{u}_{s,i}(R,z,\omega) = 0, \quad z_1 < z < D, \quad i = z,r. \quad (32)$$

In Eqs. (27) and (31), $\tilde{v}_{f,z}(r,z,\omega)$ and $\tilde{v}_{f,r}(r,z,\omega)$ correspond to the vertical and radial velocity components of the fluid, respectively.

A modal decomposition is applied both for the shell structure and the acousto-elastic waveguide. The modal expansion of the shell structure is introduced as

Redistribution subject to ASA license or copyright; see http://acousticalsociety.org/content/terms. Download to IP: 131.180.130.187 On: Mon, 30 Nov 2015 07:29:08

$$\tilde{u}_{p,j}(z,\omega) = \sum_{m=1}^{\infty} A_m U_{jm}(z). \tag{33}$$

The index $j = z, r$ indicates the corresponding displacement component, $m = 1, 2, ..., \infty$ is the axial order and the vertical eigenfunctions $U_{jm}(z)$ satisfy the chosen boundary conditions at $z = 0, L$ (any boundary conditions are allowed in this context). The expressions for the displacement and stress field in the waveguide which inherently satisfy Eqs. (22)–(30) as well as the condition at $r \to \infty$ are[4]

$$\tilde{v}_{f,z}(r,z,\omega) = \sum_{p=1}^{\infty} C_p H_0^{(2)}(k_p r)\, \tilde{v}_{f,z,p}(z), \tag{34}$$

$$\tilde{v}_{f,r}(r,z,\omega) = \sum_{p=1}^{\infty} C_p H_1^{(2)}(k_p r)\, \tilde{v}_{f,r,p}(z), \tag{35}$$

$$\tilde{p}_f(r,z,\omega) = \sum_{p=1}^{\infty} C_p H_0^{(2)}(k_p r)\, \tilde{p}_{f,p}(z), \tag{36}$$

$$\tilde{u}_{s,z}(r,z,\omega) = \sum_{p=1}^{\infty} C_p H_0^{(2)}(k_p r)\, \tilde{u}_{s,z,p}(z), \tag{37}$$

$$\tilde{u}_{s,r}(r,z,\omega) = \sum_{p=1}^{\infty} C_p H_1^{(2)}(k_p r)\, \tilde{u}_{s,r,p}(z), \tag{38}$$

$$\tilde{\sigma}_{s,zz}(r,z,\omega) = \sum_{p=1}^{\infty} C_p H_0^{(2)}(k_p r)\, \tilde{\sigma}_{s,zz,p}(z), \tag{39}$$

$$\tilde{\sigma}_{s,zr}(r,z,\omega) = \sum_{p=1}^{\infty} C_p H_1^{(2)}(k_p r)\, \tilde{\sigma}_{s,zr,p}(z), \tag{40}$$

$$\tilde{\sigma}_{s,rr}(r,z,\omega) = \sum_{p=1}^{\infty} C_p \left(H_0^{(2)}(k_p r)\, \tilde{\sigma}_{s,rr,p}^{H_0}(z) + \frac{1}{r} H_1^{(2)}(k_p r)\, \tilde{\sigma}_{s,rr,p}^{H_1}(z) \right). \tag{41}$$

In the above equations, the following stress eigenfunctions are used:

$$\tilde{\sigma}_{s,zz,p}(z) = k_p \lambda(z) \tilde{u}_{s,r,p}(z) + \rho(z) c_L^2(z) \frac{d\tilde{u}_{s,z,p}(z)}{dz}, \tag{42}$$

$$\tilde{\sigma}_{s,zr,p}(z) = G(z) \left(\frac{d\tilde{u}_{s,r,p}(z)}{dz} - k_p \tilde{u}_{s,z,p}(z) \right), \tag{43}$$

$$\tilde{\sigma}_{s,rr,p}^{H_0}(z) = k_p \rho(z) c_L^2(z) \tilde{u}_{s,r,p}(z) + \lambda(z) \frac{d\tilde{u}_{s,z,p}(z)}{dz}, \tag{44}$$

$$\tilde{\sigma}_{s,rr,p}^{H_1}(z) = -2\, G(z) \tilde{u}_{s,r,p}(z). \tag{45}$$

The functions $H_0^{(2)}(k_p r)$ and $H_1^{(2)}(k_p r)$ are the Hankel functions of the second kind of the zeroth and first order, respectively. The vertical eigenfunctions in the summation terms above, as well as the material constants, are defined explicitly over the total thickness of the waveguide by introducing the z-dependence and, therefore, the subscript index j is omitted hereafter for simplicity. The term k_p denotes the horizontal wavenumber, which is the solution of the dispersion equation formed by the set of equations (24)–(30).

In Eqs. (33)–(41) the only unknowns are the coefficients of the modal expansions A_m and C_p. A system of infinite algebraic equations with respect to the unknown coefficients C_p can be obtained by an appropriate combination of Eqs. (31) and (32) and the use of Eq. (18),[4]

$$\sum_{q=1}^{\infty} C_q \left(L_{qp} + k_q H_1^{(2)}(k_q R) \Gamma_q \delta_{qp} - \sum_{m=1}^{\infty} \frac{R_{mq} Q_{mp}}{I_m} \right) = \sum_{m=1}^{\infty} \frac{F_m Q_{mp}}{I_m}. \tag{46}$$

The coefficients of the shell structure are given by

$$A_m = \frac{F_m + \sum_{p=1}^{\infty} C_p R_{mp}}{I_m}. \tag{47}$$

The terms L_{qp}, Γ_q, Q_{mp}, R_{mp}, F_m, and I_m introduced in Eqs. (46) and (47), as well as their physical interpretation, are discussed in Tsouvalas and Metrikine.[4] In order to solve the system of infinite linear equations (46), the modal expansions of both subsystems need to be truncated. The choice of the truncation scheme is discussed in Sec. III D.

B. The complete wave spectrum of an acousto-elastic waveguide

The accurate determination of the roots k_p of the dispersion equation of the acousto-elastic waveguide is a crucial stage for the solution of the interaction problem. The dispersion equation is obtained when the determinant of the coefficient matrix, formed by the set of equations (24)–(30), is set equal to zero. In contrast to the acoustic waveguide examined in Sec. II, the solution of the dispersion equation of an elastic system has infinitely many closely spaced complex-valued roots, even for the non-dissipative case.[9] The necessity of finding modes in the complex k plane, rather than on the real or imaginary axis, makes the task of root-finding significantly more complicated.[19] To avoid any missing complex-valued roots, application of the Principle of the Argument is commonly favoured.[20–22]

A numerical algorithm for obtaining the eigenvalues k_p at each excitation frequency in the acousto-elastic layered system was written in the programming language Fortran (Intel Visual Fortran Compiler Release V11.0.062) by the authors. A detailed discussion of the algorithm falls outside the scope of the present paper. It needs only to be mentioned that it is based on the following steps: (i) A line search along the real and imaginary k-axis for locating the real and imaginary roots, respectively, based on a classical bisection algorithm,[8] and (ii) a search in the complex plane to find the values of k for which the dispersion relation turns out to be zero. The search is confined to a *narrow strip* in one of the four quadrants of the wavenumber plane (due to the isotropy of each layer's material properties), which makes the

Redistribution subject to ASA license or copyright; see http://acousticalsociety.org/content/terms. Download to IP: 131.180.130.187 On: Mon, 30 Nov 2015 07:29:08

TABLE II. Properties of the acousto-elastic waveguide consisting of an inviscid fluid layer overlying a two-layered solid.

Layer	Depth (m)	ρ (kg m^{-3})	c_L (m s^{-1})	c_T (m s^{-1})
Fluid (top)	10	1000	1500	—
Solid layer 1	15	1500	1589	142
Solid layer 2	25	1600	2213	171

algorithm computationally efficient. The search for the complex-valued roots is based on the Principle of the Argument.[23,24]

The roots of the dispersion equation for an acousto-elastic waveguide with the properties summarised in Table II are shown in Figs. 6(a) and 6(b) for two frequencies. Only the complex and imaginary roots in the fourth quadrant of the wavenumber plane with $|\mathrm{Im}(k)| \leq 10$ are shown because the complex eigenvalues occur always in pairs with the same imaginary part and real parts of opposite sign, i.e., $\pm a - \mathrm{i}b$. Wavenumbers characterised by $\mathrm{Im}(k_p) > 0$ (upper half of the wavenumber plane) are also part of the solution but are ignored in order to comply with the condition of finite response at infinite distance from the source. The following observations can be made:

(i) The complete wave spectrum for the acousto-elastic case consists of a finite number of real roots and an infinite number of complex-valued and imaginary roots;

(ii) The real roots are always top-bounded and they correspond to the propagating modes in the waveguide. The largest real-valued root corresponds to the slowest wave in the medium. This root is similar to that of the conventional *Scholte* wave for sufficiently large frequency (or equivalently large depth of the waveguide);

(iii) The complex-valued roots are positioned close to the imaginary axis and are clustered into two branches. The number of branches is equal to the number of the solid layers compiling the waveguide. This can be concluded from the vertical eigenfunctions belonging to wavenumbers of a particular branch which have the largest amplitude in one of the solid layers. The two branches are clearly marked only for $f = 10$ Hz. At higher frequencies, the two branches move closer to the imaginary axis. At a frequency of 100 Hz the branches are indistinguishable;

(iv) The majority of the imaginary roots correspond to evanescent modes which introduce significant motion in the fluid layer. It has been observed (although not shown explicitly here) that a few imaginary roots correspond to modes with significant amplitude in the solid part of the waveguide. These roots are related to those dispersion curves that (through the complex wavenumber plane) follow a *short path* via the imaginary axis for increasing frequency before turning into propagating modes.

C. The complete wave spectrum of an elastic waveguide

Although the present paper is perhaps not the most appropriate place for a complete discussion on the subject, it is of interest to highlight once the differences between an elastic and an acousto-elastic waveguide, focusing on the complete wave spectrum. To investigate the influence of the presence of the fluid layer on the position of the complex-valued and imaginary roots, an analysis is performed in which the fluid layer is absent and the properties of the solid layers are those given in Table II. The obtained roots for the elastic and acousto-elastic cases are plotted together in Fig. 7 for comparison. Complex and imaginary roots with

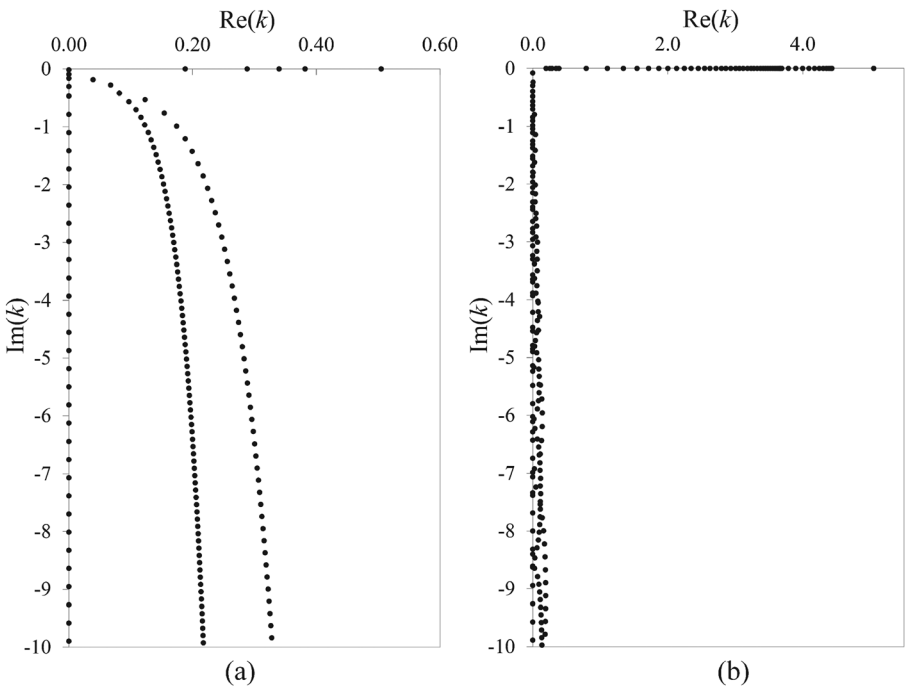

FIG. 6. Roots of the dispersion equation for the acousto-elastic waveguide with the properties given in Table II at (a) $f = 10$ Hz and (b) $f = 100$ Hz. The propagating modes are all positioned on the real axis. The evanescent modes are positioned either on the imaginary axis or on the third and fourth quadrant of the complex wavenumber plane. Only the complex roots in the fourth quadrant are shown here because of symmetry considerations.

Redistribution subject to ASA license or copyright; see http://acousticalsociety.org/content/terms. Download to IP: 131.180.130.187 On: Mon, 30 Nov 2015 07:29:08

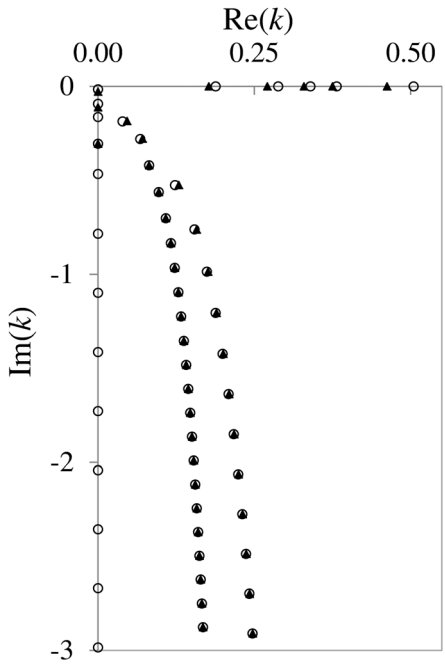

FIG. 7. Roots of the dispersion equation at $f = 10$ Hz for the acousto-elastic waveguide (empty circles) with the properties given in Table II and for the elastic one (filled triangles) in which the upper fluid layer is absent. The position of the real roots and of a few complex-valued roots is modified due to the presence of the fluid layer; only the complex-valued roots, which induce significant motion in the upper solid layer, are influenced by the presence of the fluid layer.

$|\mathrm{Im}(k)| > 3$ are excluded from Fig. 7. The following points are worth noticing:

(i) The presence of the fluid layer modifies the position of the real-valued roots. In fact, there is a slight shift of all wavenumbers toward larger values in the acousto-elastic case. The phase speed of the Scholte mode (acousto-elastic waveguide) is smaller than the one of the Rayleigh mode (elastic waveguide). It can be shown that at higher frequencies, additional real-valued roots appear in the acousto-elastic waveguide which are associated with propagating modes with significant motion in the fluid layer. Obviously, the latter ones do not have any counterparts in the elastic case;

(ii) The presence of the acoustic layer exposes an infinite set of imaginary roots. Most of these roots correspond to modes with significant amplitudes in the fluid layer. In the elastic case, the amount of imaginary roots is always finite and they correspond to modes that follow a *short path* via the imaginary axis for increasing frequency before turning into propagating modes (Sec. III B);

(iii) The complex-valued roots correspond to modes with significant motion induced in the solid layers. The position of few *shallow roots* of the outer branch (the complex ones with a small imaginary part that induce significant motion in the upper solid layer) are modified due to the presence of the fluid layer. The position of the rest of the complex-valued roots remains largely unaffected by the presence of the fluid.

D. Convergence of the displacement and stress fields

Having analysed the complete wave spectrum of an acousto-elastic waveguide, the importance of the evanescent field for the shell-waveguide interaction problem is now addressed. The material and geometrical properties of the waveguide are already given in Table II and those of the shell structure are defined as follows: $E = 210\,000$ MPa, $\tilde{v} = 0.28$, $\rho = 7850$ kg m^{-3}, $R = 2.7$ m, $L = D = 58$ m, $2h = 0.05$ m, $z_0 = 8$ m, $z_1 = 18$ m, and $z_2 = 33$ m. The force applied at the pile head is equal to $|\tilde{F}(\omega)| = 10^6$ N s. In the results shown hereafter, the number of shell modes are 400, which is regarded as sufficient for the frequency range of interest.

The convergence of the solution is examined in terms of the displacement mismatch error at the interface $r = R$ and along $z_0 \le z \le L$, i.e.,

$$\delta_j(z) = \left| \frac{\tilde{u}_{p,j}(z,\omega) - \tilde{u}_{s:f,j}(R,z,\omega)}{\tilde{u}_{p,j}(z,\omega)} \right|, \tag{48}$$

with $j = r, z$ for the radial and vertical displacement mismatch, respectively. The average error along the length of the shell, i.e., $\hat{\delta}_j = \langle \delta_j(z) \rangle$, is used hereafter as the error criterion for the convergence of the displacements at the interface. The error for the radial displacements is examined separately for the portion of the pile in contact with the fluid layer ($z_0 \le z \le z_1$) and for the portion embedded into the soil ($z_1 < z < L$). As explained previously, the majority of the imaginary roots correspond to evanescent modes with significant amplitude in the fluid region, whereas the complex-valued roots correspond to modes with significant amplitude in the soil region. It is therefore expected that the convergence of the solution in the two regions (fluid and solid) will be governed by a different set of evanescent modes.

In Fig. 8, $\hat{\delta}_r$ and $\hat{\delta}_z$ are plotted versus the number of evanescent modes at a fixed frequency. In general, $\hat{\delta}_z$ is lower than $\hat{\delta}_r$ in all cases. The radial displacement continuity

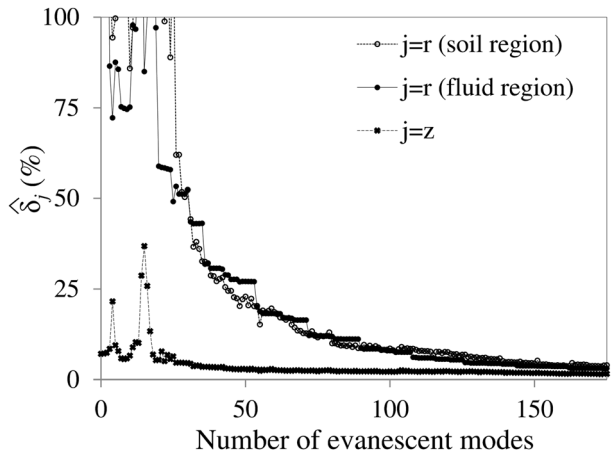

FIG. 8. Mismatch error $\hat{\delta}_j(\%)$ for the different displacement components as a function of the number of the evanescent modes at $f = 10$ Hz for the case of a shell coupled to an acousto-elastic waveguide. Similar results are obtained in other frequencies as well and are omitted here for the sake of brevity. The inclusion of more than 100 evanescent modes is required to reduce the average displacement mismatch of all components to a value <10%.

Redistribution subject to ASA license or copyright; see http://acousticalsociety.org/content/terms. Download to IP: 131.180.130.187 On: Mon, 30 Nov 2015 07:29:08

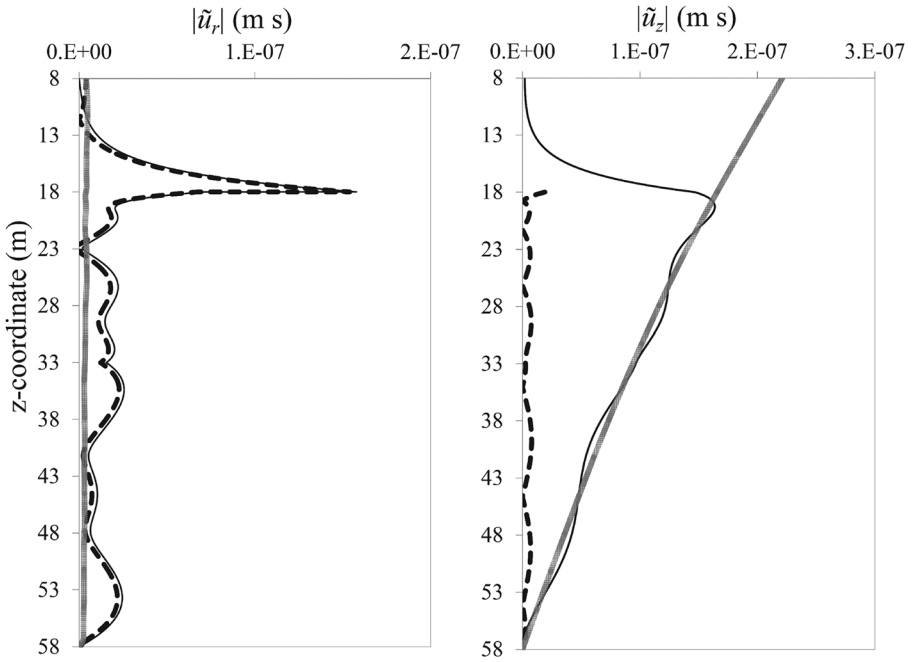

FIG. 9. Displacements of the shell and of the waveguide at $f = 10$ Hz when only propagating modes are considered. The left figure shows the radial displacement mismatch, whereas the right figure shows the vertical displacement mismatch. The thin line denotes the displacement of the waveguide, the thick (grey) line denotes the displacement of the shell structure, and the dashed line denotes the mismatch of these two. The vertical displacement continuity is satisfactory at the interface. On the contrary, the radial displacements do not match.

at the soil and fluid regions converges much slower due to the error introduced at the horizontal surfaces and interfaces $z = z_0$, $z = z_1$, and $z = z_2$. In these positions, a sharp change in the material properties of the waveguide is present (interface between adjacent layers). Sharp horizontal discontinuities are difficult to be described by modal approximations and therefore a large number of evanescent modes are required for convergence.

In Fig. 9, the displacement of the shell structure and that of the exterior domain at $f = 10$ Hz are plotted together when only propagating modes are considered for the waveguide. Note that for the domain $z_0 \leq z \leq z_1$ no mismatch is plotted for the vertical displacements (the fluid is assumed inviscid). As can be seen, the displacement mismatch at the interface is satisfactory only for the vertical displacement component. The predicted radial displacement field in the waveguide is incorrect when only propagating modes are considered and is significantly over-predicted (as can be seen in Fig. 10).

In Fig. 10, the same plots are shown but now the evanescent field is accounted for. Clearly, an increasing number of evanescent modes yields an improved satisfaction of the kinematic compatibility at the shell-fluid and shell-soil interface. The mismatch of the vertical displacement component at the interface is much smaller compared to the radial mismatch, but the latter converges as well with the inclusion of an increasing number of evanescent modes. The displacement error is mainly governed by the errors introduced at the horizontal surface $z = z_0$ and interface $z = z_1$. The convergence of the radial displacements at $z = z_2$, i.e., the interface between the soil layers, is regarded as satisfactory $[\delta_r(z_2) \leq 1\%]$ when

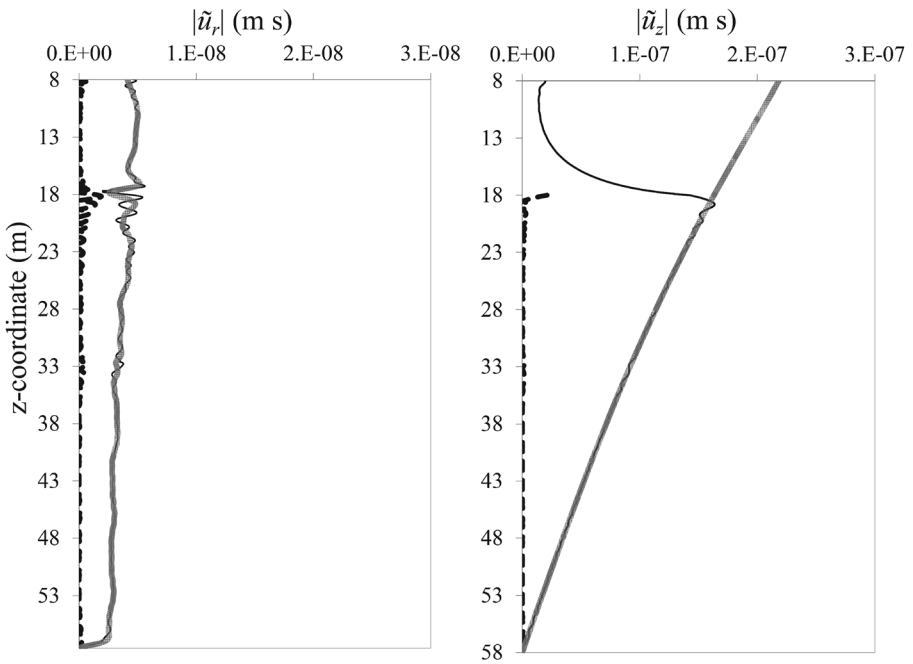

FIG. 10. Displacements of the shell and of the waveguide at $f = 10$ Hz with the inclusion of 184 evanescent modes for the acousto-elastic waveguide. The left figure shows the radial displacement mismatch, whereas the right figure shows the vertical displacement mismatch. The thin line denotes the displacement of the waveguide, the thick (grey) line denotes the displacement of the shell structure, and the dashed line denotes the mismatch. The inclusion of the evanescent regime improves the satisfaction of the interface conditions.

Redistribution subject to ASA license or copyright; see http://acousticalsociety.org/content/terms. Download to IP: 131.180.130.187 On: Mon, 30 Nov 2015 07:29:08

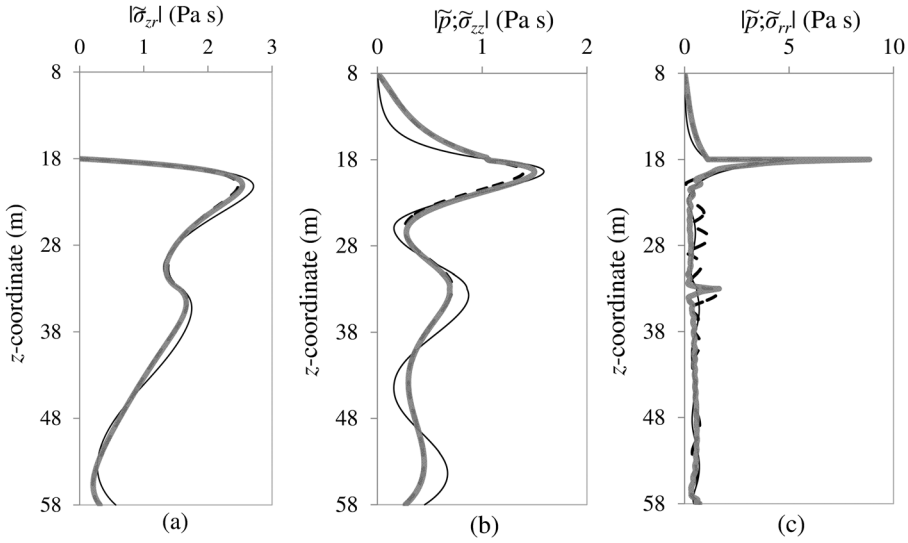

FIG. 11. Stress field in the waveguide at $r=R$ for $f=10$ Hz. (a) The stress amplitude $\tilde{\sigma}_{zr}$ along the length of the shell structure is shown. Similarly, (b) and (c) show the stress components $\tilde{\sigma}_{zz}$ and $\tilde{\sigma}_{rr}$. In each part, the black line denotes the stress field when only propagating modes are considered. The dashed line corresponds to the case in which 30 evanescent modes are included. The thick grey line corresponds to the case in which 184 evanescent modes are considered. The stress components $\tilde{\sigma}_{zr}$ and $\tilde{\sigma}_{zz}$ converge relatively fast [(a) and (b)]. On the contrary, the stress component $\tilde{\sigma}_{rr}$ requires a large part of the evanescent spectrum for a satisfactory convergence at $z=z_1$.

more than 100 evanescent modes are included. On the contrary, the radial displacement error at $z=z_0$ is then on the order of 10% and converges much slower.

In Figs. 11(a)–11(c), the stresses generated at the pile-waveguide interface are shown for a varying number of evanescent modes considered in the solution. As can be seen, the convergence of the stress components $\tilde{\sigma}_{zr}$ [Fig. 11(a)] and $\tilde{\sigma}_{zz}$ [Fig. 11(b)], as well as the fluid pressure is satisfactory with the inclusion of a few evanescent modes. On the contrary, the stress $\tilde{\sigma}_{rr}$ converges much slower and requires a large number of evanescent modes. Again, the slow convergence of the field in this last case is mainly caused by the *sharp* change in the material properties at the horizontal interfaces $z=z_2$.

E. Convergence of the solution in terms of energy radiation

As discussed in Sec. II, the error in the coefficients of the propagating modes is related to the error in the energy radiation into the waveguide. In Fig. 12, the error in the calculation of the coefficients of the propagating modes, i.e., Eq. (17), is shown at $f=10$ Hz (five propagating modes in this case). Clearly, a large number of evanescent modes is required for convergence of coefficient C_1. Nevertheless, it should be noted that $|C_1^q|$ is several orders of magnitude smaller compared to the other coefficients. This implies that the particular mode is not significantly excited at this frequency. Thus, the introduced error $\delta_{p,1}$ is insignificant for the overall response of the system. An estimation of the coefficients for the other propagating modes ($m=2,\ldots,5$) within an accuracy of $<5\%$ requires <100 evanescent modes. Similar plots are obtained for other frequencies and are omitted here for the sake of brevity. In general, the exact satisfaction of the shell-waveguide interface conditions guarantees the convergence of the solution in terms of energy radiation into the surrounding media. In contrast, the convergence of the solution in terms of energy radiation (coefficients of the propagating modes only) does not *per se* guarantee the strict satisfaction of the kinematic conditions at the shell-waveguide interface. Thus, if accurate predictions of the displacement and stress fields at the interface are required, one should avoid the adoption of convergence criteria for the truncation of the waveguide modes that are based solely on energy radiation considerations. Adopting convergence criteria that are based on the satisfaction of the kinematic conditions at the shell-waveguide interface seems to be more appropriate in this context because they provide the necessary error control in the estimation of the coefficients of the evanescent modes.

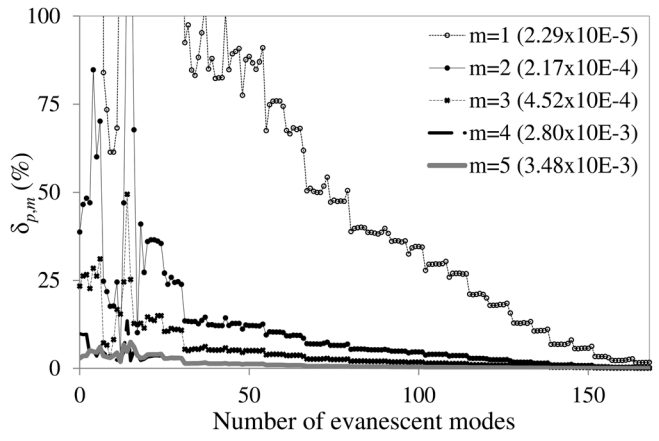

FIG. 12. Error percentage $\delta_{p,m}(\%)$ for the coefficients of the propagating modes at $f=10$ Hz. The amplitude of the each coefficient as obtained by the exact solution to the problem is shown in the parenthesis. The slow convergence of $\delta_{p,1}$ does not influence the resulting displacement and stress fields due to the small amplitude of the correspondent mode, i.e., the particular mode is not excited by the load at this frequency. The rest of the coefficients converge to within an error $\delta_{p,m}\leq 5\%$ when more than 90 evanescent modes are included.

IV. WAVE RADIATION GENERATED BY OFFSHORE PILE DRIVING

In the present section, the convergence criteria established previously are applied to the case of a pile being driven into the soil offshore. The satisfaction of the displacement and stress continuity at the pile-waveguide interface, by using the criteria established in Sec. III, allows for an accurate estimation of the intensity of the acoustic field very close to the pile surface. The generation and propagation of the waves in the water-soil domain is examined for the case of impact pile

Redistribution subject to ASA license or copyright; see http://acousticalsociety.org/content/terms. Download to IP: 131.180.130.187 On: Mon, 30 Nov 2015 07:29:08

driving. This particular problem is of great importance for the offshore industry since pile driving and structure-borne wave radiation into the marine environment are closely related to underwater noise pollution.[13–16] In this context, realistic models for the prediction of the underwater noise levels are needed. The theoretical framework of such a model is already given in Sec. III. A detailed investigation of the dynamics of the coupled pile-water-soil system for the case of a single soil layer is discussed in Tsouvalas and Metrikine.[4] In the aforementioned publication, the chosen soil properties were based on an elastic medium with $c_L/c_T \sim 3$, which is not always representative of an unconsolidated marine sediment. The latter is typically characterised by larger values of the velocity ratio due to water saturation.[25]

The marine sediment is traditionally described by an equivalent fluid for the modeling of underwater acoustics generated by pile driving.[26–28] More advanced methods for the description of unconsolidated marine sediments do exist. These can be divided into three primary groups. The first group treats the offshore soil as a classical elastic continuum with modified properties to account for water saturation. The second group belongs to the so-called grain-shearing model, indented to represent wave propagation in unconsolidated granular media, in which the mineral grains are in contact but unbonded.[29] The last group treats the continuum as a poroelastic medium and is based on the well-established theory of Biot.[30,31]

In the case of offshore pile driving, a few points need to be mentioned additionally. First, it is well known that almost all marine sediments possess enough shear rigidity to transmit shear waves, which can be important in underwater sound propagation because compressional waves can be partially converted to shear, Scholte, and Stoneley waves at reflection boundaries. Second, the acoustic approximation for the modeling of a solid can be considered reliable when (i) The energy is released in the fluid region and only the radiated field in the fluid domain is required; (ii) The *source* and *receiver* are not positioned close to (or at) the sea bottom, so that the shear waves and interface modes of propagation do not dominate the response;[32] (iii) The dynamics of the soil region does not influence the radiating source itself. Obviously, in the case of pile driving, none of the aforementioned conditions is sufficiently met. Third, a realistic solution of the interaction problem becomes essential for the correct determination of the energy distribution among the various subsystems, i.e., pile, water, and marine sediment. With respect to this last point, the focus should not only be placed on the description of wave propagation in the acousto-elastic medium that surrounds the pile, but also on the pile-waveguide interaction problem. Defining an appropriate model for the former purpose does not *per se* guarantee the suitableness of that same model for the latter one. Thus, even though fluid approximations of the seabed are commonly favoured in computational acoustics, in the case of pile driving, somewhat more sophisticated models may be required.

Results are presented hereafter in which the marine sediment is modeled as a layered elastic medium with modified properties to account for water saturation based on the works of Hamilton[25] and Buckingham.[33] The soil sediment is divided into two layers, namely, an upper layer of *fine sand* that overlies a layer compiled of a mixture of sand, clay, and silt (Table III). The properties of the two layers are obtained from Tables IB and VIB and Figs. 7 and 16 of Hamilton,[25] taking into account the related work of Buckingham.[33] The values α_p and α_s shown in Table III denote the attenuation of the compressional and shear waves in each layer. The material properties of the pile are given in Sec. III with merely a change of $z_0 = 5$ m and $z_1 = 23$ m. An impulsive force is applied at the head with a maximum amplitude of 1.2×10^8 N and a pulse duration of $\sim$0.005 s. This corresponds, approximately, to a hammer energy input of 1000 kJ.

In Fig. 13, the wave radiation into the soil and into the water column is shown at several time moments after the hammer impact. Due to the symmetry of the loading conditions and the geometry, only the r-z plane is shown in Fig. 13, i.e., the response is cylindrically symmetric. The pressure distribution in the fluid region is shown in the upper part ($z \leq 23$ m), whereas in the lower part ($z > 23$ m) the norm of the particle velocity vector is depicted. The following general observations need to be mentioned:

(i) The response in the fluid region consists of compressional waves (pressure wave fronts) with an inclination of $\sim$16° to the vertical. This is in full agreement with results presented elsewhere;[3,26,27]

(ii) The response in the soil region consists of both shear and compressional waves. In the upper soil layer, the compressional waves have a speed which is larger than the speed of the bulk waves in the water ($c_{L,1} > c_f$) and therefore a slightly larger inclination to the vertical is observed. Shear wave fronts are also formed with almost vertical polarisation due to the large contrast between the velocity of the compressional waves in the pile ($c_p \simeq 5400$ ms^{-1}) and the shear wave speeds in the soil ($c_T \leq 200$ ms^{-1}). At the interface between the two soil layers, the inclination of the shear fronts increases in the lower soil medium because $c_{T,1} < c_{T,2}$. The main difference with respect to the cases analysed in Tsouvalas and Metrikine[4] is that in the present case, the compressional waves in the soil propagate with speeds that are comparable to the ones of the pressure waves in the fluid region. At the interface between the two solids, the wave field is distorted due to the difference in the shear wave speeds between the two media and the possible existence of a Stoneley wave;

(iii) Scholte waves are generated at the seabed-water interface. Their amplitudes decrease with increasing

TABLE III. Acousto-elastic waveguide consisting of three layers (from top to bottom): water column, fine-sand layer, and a sand-clay-silt layer. Properties derived from Tables IB and VIB and Figs. 7 and 16 of Hamilton (Ref. 25), taking into account the related work of Buckingham (Ref. 33).

Layer	Depth m	ρ kg m^{-3}	c_L m s^{-1}	c_T m s^{-1}	α_p dB m^{-1} kHz^{-1}	α_s dB m^{-1} kHz^{-1}
Water	18	1023	1453	—	—	—
Fine sand	10	1900	1797	113	0.40	15.0
Sand-silt-clay	25	1780	1635	175	0.30	13.0

Redistribution subject to ASA license or copyright; see http://acousticalsociety.org/content/terms. Download to IP: 131.180.130.187 On: Mon, 30 Nov 2015 07:29:08

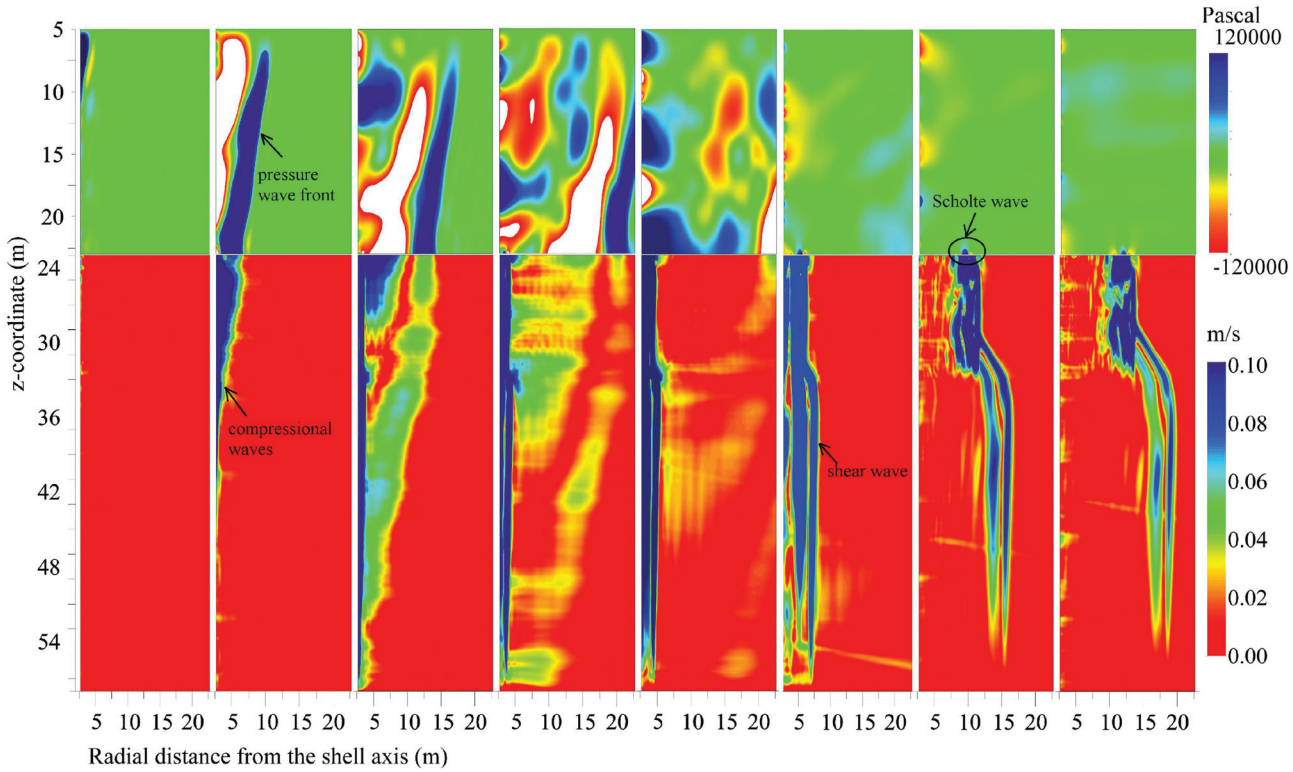

FIG. 13. Pressures in the fluid ($z \leq 23$; top) and velocity norm in the soil ($z > 23$; bottom) for several moments in time after the hammer impact. From left to right, the time moments are given in 10^{-3} s: $t = 8.4$; 13.2; 18; 22.8; 27.6; 42; 90; 108. The wave field in the water consists of pressure cones as indicated in the figure. The field in the soil consists of compressional and shear wave fronts. The compressional waves in the soil propagate with a speed similar to that of the bulk waves in the fluid region. Scholte waves (indicated by the black circle) are generated at the seabed-water interface and are visible from $t > 42 \times 10^{-3}$ s onward. The Scholte waves induce low-frequency pressure fluctuations close to the seabed.

distance from the interface and with increasing range from the pile surface. Nevertheless, it should be pointed out that even at a distance of 20 m from the pile surface, the pressure amplitudes induced by the Scholte wave in the fluid region and in the vicinity of the seabed level are ~80 kPa in this particular case; a magnitude comparable to the one induced by the fluid body waves.

The contribution of the Scholte waves for a point positioned 1 m above the seabed surface is shown in Fig. 14 for three distances from the surface of the pile. As can be seen, the radial velocity field for points positioned close to the seabed consists of two separate contributions. At the initial moments in time, the pressure cones, traveling with the speed of sound in the fluid region, contribute to the radial velocities, whereas at later time moments the Scholte waves dominate the velocity field close to the seabed. For points positioned a few wavelengths away from the seabed surface, the latter contribution can naturally be neglected.

It should also be noted that the energy transferred into the Scholte wave is smaller when compared to the results of an equivalent *dry soil* presented in Tsouvalas and Metrikine[4] as pointed out in Lippert and von Estorff.[28] However, this does not imply that the Scholte wave is unimportant in this context. As discussed, its contribution can be significant, even at distances of several wavelengths away from the surface of the pile. In addition, it has been observed[4] that the energy *carried* by the shear and Scholte waves is a function of several parameters, i.e., the waveguide properties, the type of dynamic excitation, the diameter of the pile, etc. Naturally, the contribution of the Scholte waves is restricted to the vicinity of the seabed-water interface. Nevertheless, to the best of the authors' knowledge, it would be very difficult for one to *a priori* judge whether this contribution is negligibly small, let alone to define the domain influenced by the interface waves.

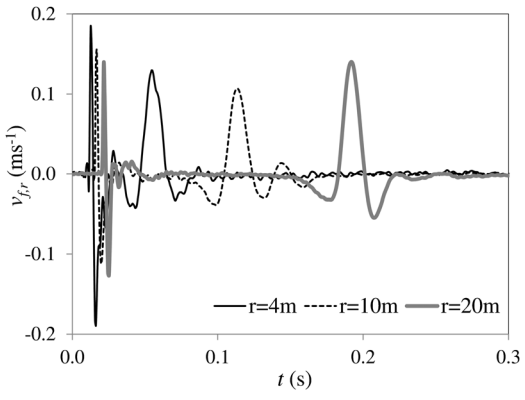

FIG. 14. Evolution of the radial velocity field with time for a point positioned 1 m above the seabed surface and at several horizontal positions. The field consists of two contributions. The early contribution ($t < 0.05$ s) is attributed to the bulk waves in the fluid, which are radiated directly from the vibrations of the shell surface. The second contribution is attributed to the Scholte waves, which induce low-frequency oscillations close to the seabed-water interface.

Redistribution subject to ASA license or copyright; see http://acousticalsociety.org/content/terms. Download to IP: 131.180.130.187 On: Mon, 30 Nov 2015 07:29:08

V. CONCLUDING REMARKS

In this contribution, the significance of the evanescent spectrum for the solution of structure-waveguide interaction problems was discussed. The emphasis was placed on the dynamic response of the structure and on the generated displacement and stress fields at the structure-waveguide interface. Two examples were analysed, namely, a beam in contact with a fluid layer and a cylindrical shell embedded in a layered acousto-elastic waveguide. For each of the aforementioned problems, a solution method is presented which is based on the modal decomposition of the separate fields, i.e., those in the structure and in the waveguide, into complete sets of orthogonal eigenfunctions. Once the eigenmodes of the two subsystems are known, the orthogonality relations are utilised at their interface for the satisfaction of the imposed kinematic continuities. This yields an infinite set of coupled algebraic equations which can be solved only when the infinite summations are truncated.

Appropriate truncation criteria that guarantee the convergence of the solution to within a predefined error margin were establishment. Convergence criteria that are based solely on energy considerations are shown to be inappropriate for the accurate determination of the forces and displacements in the structure due to the fact that they do not reflect possible calculation errors in the amplitudes of the evanescent modes. In fact, the accurate determination of the amplitudes of the latter is essential for the prediction of the dynamic response of the coupled system in terms of displacements and stress at the structure-waveguide interface.

In the last section of the manuscript, the wave radiation into the fluid-soil region generated by a steel monopile being driven into the soil offshore was discussed. The previously established truncation criteria allowed the examination of the generated wave field at the vicinity of the pile surface. This particular example was analysed to some detail because it received recently the attention of the scientific community. Sound radiation generated during the installation of piles emits strong impulsive sounds into the seawater column, which can be harmful for the marine ecosystem. In contrast to other studies, the marine sediment is described as a layered elastic continuum with modified properties to account for water saturation. Thus, the co-existence of shear and compressional waves is allowed together with the associated interface modes. Once a set of realistic properties for the marine sediment are defined, the wave field generated by an impact of the hammer is analysed. The contribution of the shear and Scholte waves in the overall response of the coupled pile-water-soil system is emphasised. In contrast to the common opinion, the presence of the shear and closely related Scholte waves cannot be neglected in this particular problem due to their significant contribution to the solution of the coupled system and their influence on the low-frequency oscillations at the vicinity of the sea floor.

ACKNOWLEDGMENTS

A.T. would like to acknowledge FLOW (Far and Large Offshore Wind farms) for financing the research on underwater noise generated by offshore pile driving. K.N.v.D. was sponsored by the TKIW02001 project on Dynamic Soil-Structure Interaction. Finally, the authors would like to thank their colleague Jeroen Hoving for computational assistance regarding the development of the complex root-finder in Fortran.

[1]G. Shkerdin and C. Glorieux, "Lamb mode conversion in an absorptive bi-layer with a delamination," J. Acoust. Soc. Am. **118**(4), 2253–2264 (2005).
[2]G. Shkerdin and C. Glorieux, "Interaction of lamb modes with delaminations in plates coated by highly absorbing materials," IEEE Trans. Ultrason., Ferroelectr., Freq. Control **54**(2), 368–377 (2007).
[3]A. Tsouvalas and A. V. Metrikine, "A semi-analytical model for the prediction of underwater noise from offshore pile driving," J. Sound Vib. **332**(13), 3232–3257 (2013).
[4]A. Tsouvalas and A. V. Metrikine, "A three-dimensional vibroacoustic model for the prediction of underwater noise from offshore pile driving," J. Sound Vib. **333**(8), 2283–2311 (2014).
[5]S. Stange and W. Friederich, "Guided wave propagation across sharp lateral heterogeneities: The complete wavefield at a cylindrical inclusion," Geophys. J. Int. **111**(3), 470–482 (1992).
[6]S. Stange and W. Friederich, "Guided wave propagation across sharp lateral heterogeneities: The complete wavefield at plane vertical discontinuities," Geophys. J. Int. **109**(1), 183–190 (1992).
[7]K. Aki and P. G. Richards, *Quantitative Seismology*, 2nd ed. (University Science Books, Sausalito, CA, 2002), 700 pp.
[8]F. B. Jensen, W. A. Kuperman, M. B. Porter, and H. Schmidt, *Computational Ocean Acoustics* (Springer, Heidelberg, 2012), pp. 337–454.
[9]J. D. Achenbach, "Wave propagation in elastic solids," in *North-Holland Series in Applied Mathematics and Mechanics*, edited by H. A. Lauwerier and W. T. Koiter (North-Holland, Amsterdam, 1973), pp. 226–236.
[10]B. Karp and D. Durban, "Evanescent and propagating waves in prestretched hyperelastic plates," Int. J. Solids Struct. **42**(5–6), 1613–1647 (2005).
[11]G. Shkerdin and C. Glorieux, "Interaction of lamb modes with an inclusion," Ultrasonics **53**(1), 130–140 (2013).
[12]B. Nennig, E. Perrey-Debain, and M. Ben Tahar, "A mode matching method for modeling dissipative silencers lined with poroelastic materials and containing mean flow," J. Acoust. Soc. Am. **128**(6), 3308–3320 (2010).
[13]P. T. Madsen, M. Wahlberg, J. Tougaard, K. Lucke, and P. Tyack, "Wind turbine underwater noise and marine mammals: Implications of current knowledge and data needs," Mar. Ecol.: Prog. Ser. **309**, 279–295 (2006).
[14]J. A. David, "Likely sensitivity of bottlenose dolphins to pile-driving noise," Water Environ. J. **20**(1), 48–54 (2006).
[15]H. Bailey, B. Senior, D. Simmons, J. Rusin, G. Picken, and P. M. Thompson, "Assessing underwater noise levels during pile-driving at an offshore windfarm and its potential effects on marine mammals," Mar. Pollut. Bull. **60**(6), 888–897 (2010).
[16]C. Erbe, "International regulation of underwater noise," Acoust. Aust. **41**(1), 12–19 (2013).
[17]K. F. Graff, "Wave motion in elastic solids," in *Dover Books on Engineering Series* (Dover Publications, New York, 1975), pp. 155–170.
[18]J. D. Kaplunov, L. Y. Kossovich, and E. V. Nolde, *Dynamics of Thin Walled Elastic Bodies* (Academic, San Diego, 1998), pp. 116–140.
[19]E. K. Westwood, C. T. Tindle, and N. R. Chapman, "A normal mode model for acousto-elastic ocean environments," J. Acoust. Soc. Am. **100**(6), 3631–3645 (1996).
[20]L. M. Delves and J. N. Lyness, "A numerical method for locating the zeros of an analytic function," Math. Comput. **21**(100), 543–560 (1967).
[21]X. Ying and I. N. Katz, "A reliable argument principle algorithm to find the number of zeros of an analytic function in a bounded domain," Numer. Math. **53**(1–2), 143–163 (1988).
[22]C. Gillan, A. Schuchinsky, and I. Spence, "Computing zeros of analytic functions in the complex plane without using derivatives," Comput. Phys. Commun. **175**(4), 304–313 (2006).
[23]M. Dellnitz, O. Schtze, and Q. Zheng, "Locating all the zeros of an analytic function in one complex variable," J. Comput. Appl. Math. **138**(2), 325–333 (2002).

Redistribution subject to ASA license or copyright; see http://acousticalsociety.org/content/terms. Download to IP: 131.180.130.187 On: Mon, 30 Nov 2015 07:29:08

[24]T. Johnson and W. Tucker, "Enclosing all zeros of an analytic function: A rigorous approach," J. Comput. Appl. Math. **228**(1), 418–423 (2009).
[25]E. L. Hamilton, "Geoacoustic modeling of the sea floor," J. Acoust. Soc. Am. **68**(5), 1313–1340 (1980).
[26]P. G. Reinhall and P. H. Dahl, "Underwater mach wave radiation from impact pile driving: Theory and observation," J. Acoust. Soc. Am. **130**(3), 1209–1216 (2011).
[27]M. Zampolli, M. J. J. Nijhof, C. A. F. de Jong, M. A. Ainslie, E. H. W. Jansen, and B. A. J. Quesson, "Validation of finite element computations for the quantitative prediction of underwater noise from impact pile driving," J. Acoust. Soc. Am. **133**(1), 72–81 (2013).
[28]T. Lippert and O. von Estorff, "The significance of parameter uncertainties for the prediction of offshore pile driving noise," J. Acoust. Soc. Am. **136**(5), 2463–2471 (2014).
[29]M. J. Buckingham, "Wave propagation, stress relaxation, and grain-to-grain shearing in saturated, unconsolidated marine sediments," J. Acoust. Soc. Am. **108**(6), 2796–2815 (2000).
[30]M. A. Biot, "Theory of propagation of elastic waves in a fluid saturated porous solid: I. Low frequency range," J. Acoust. Soc. Am. **28**(2), 168–178 (1956).
[31]M. A. Biot, "Theory of propagation of elastic waves in a fluid saturated porous solid: II. Higher frequency range," J. Acoust. Soc. Am. **28**(2), 179–191 (1956).
[32]Z. Y. Zhang and C. T. Tindle, "Improved equivalent fluid approximations for a low shear speed ocean bottom," J. Acoust. Soc. Am. **98**(6), 3391–3396 (1995).
[33]M. J. Buckingham, "Compressional and shear wave properties of marine sediments: Comparisons between theory and data," J. Acoust. Soc. Am. **117**(1), 137–152 (2005).

Redistribution subject to ASA license or copyright; see http://acousticalsociety.org/content/terms. Download to IP: 131.180.130.187 On: Mon, 30 Nov 2015 07:29:08